International Journal of Thermal Sciences 49 (2010) 643–652

Contents lists available at ScienceDirect

International Journal of Thermal Sciences

journal homepage: www.elsevier.com/locate/ijts

Investigation of heat transfer and bubble dynamics in a boiling thin liquid film flowing over a rotating disk

G. Quinn*, B.M. Cetegen

University of Connecticut, Department of Mechanical Engineering, 191 Auditorium Road, Unit 3139, Storrs, CT-06269-3139, USA

ARTICLE INFO

Article history:
Received 19 February 2009
Received in revised form
4 September 2009
Accepted 6 September 2009
Available online 25 September 2009

Keywords:
Heat transfer
Jet impingement
Boiling
Rotating disk
Integral analysis

ABSTRACT

Nucleate boiling heat transfer and bubble dynamics in a thin liquid film on a horizontal rotating disk were studied. A series of experiments were conducted to determine the heat transfer coefficient on the disk. At low rotation and flow rates, vigorous boiling increased the heat transfer coefficients above those without boiling. Higher rotational speeds and higher flow rates increased the heat transfer coefficient and suppressed boiling by decreasing the superheat in the liquid film. The flow field on the disk, which included supercritical (thin film) flow upstream of a hydraulic jump, and subcritical (thick film) flow downstream of a hydraulic jump, affected the type of bubble growth. Three types of bubble growth were identified. Vigorous boiling with large, stationary bubbles were observed in the subcritical flow. Supercritical flow produced small bubbles that remained attached to the disk and acted as local obstacles to the flow. At low rotational rates, the hydraulic jump that separated the supercritical and subcritical regions produced hemispherical bubbles that protruded out of the water film surface and detached from the disk, allowing them to slide radially outward. A model of the velocity and temperature of the microlayer of water underneath these sliding bubbles indicated that the microlayer thickness was approximately 1/25th of that of the surrounding water film. This microlayer is believed to greatly enhance the heat transfer rate underneath the sliding bubbles.

1. Introduction

Thermal transport is becoming the limiting factor in adding capabilities to new aircraft and spacecraft systems. One of the key objectives for effective thermal management is the improvement of heat transport and rejection. It is anticipated that heat pumping will become necessary to accommodate the increasing thermal loads in future aerospace systems [1]. One possibility to meet this need for spacecraft applications is to create a micro-gravity compatible vapor absorption heat pump. Such a heat pump would allow spacecraft to maintain thermal stability while rejecting heat at higher temperatures, thus allowing the use of smaller radiators, sublimators or evaporators. Vapor absorption heat pumps merit investigation for spacecraft cooling due to their high efficiency.

Vapor absorption heat pumps can be made even more efficient by using several mechanisms to improve convective heat transfer in the generator section of the system, including liquid jet impingement, thin liquid film heat transfer and nucleate boiling. The combination of using a boiling thin liquid film with film acceleration imparted by rotation may be ideal for micro-gravity applications. A rotating disk manages the fluid dynamics in micro-gravity and thins it out for enhanced heat transfer at the same time. Nucleate boiling on a rotating disk further enhances heat transfer.

The problem of characterizing heat transfer rates of boiling fluids in rotating flow has been addressed in the literature. One important field is the cooling of gas turbine engines where effective cooling in centrifugal fields is applicable to turbine blade cooling. Better heat transfer between the blades and their internal coolant flow can allow for hotter combustion temperatures and thus increases in the efficiency of the gas turbine, as explained in Mudawwar and El-Masri [2]. They investigated incipient boiling heat flux in thin rotating films, which is applicable to turbine blade cooling. Their test apparatus consisted of a water jet impinging axially on a rotating surface. Water was collected in a spiral channel before being flung over a radially oriented heater surface. Boiling heat transfer data were gathered and it was found that the increased acceleration of the flow delayed the onset of boiling by increasing the convective heat transfer coefficient. Surface roughness and Coriolis forces also played a role on the onset of boiling.

Yanniotis and Kolokotsa [3] conducted boiling experiments with water dispersed on a horizontal, rotating disk, with the goal of better understanding centrifugal evaporators for use in process intensification. They used a 30 cm diameter disk with a water distribution collar at the center for a range of water flow rates and

* Corresponding author. Tel.: +1 860 654 9325; fax: +1 860 660 3742.
E-mail address: gregory.quinn@hs.utc.com (G. Quinn).

1290-0729/$ – see front matter © 2009 Elsevier Masson SAS. All rights reserved.
doi:10.1016/j.ijthermalsci.2009.09.001

Nomenclature

A	Bubble analysis variable
A_h	Area of the heater, m^2
A_i	Local Area, m^2
B	Bubble analysis variable
C	Bubble analysis variable
h_i	Local heat transfer coefficient, $(\dot{Q}/A_h)/(T_{wi}-T_o)$, W m^{-2} K^{-1}
h_o	Height of controlled jet at the exit of the collar, m
k_l	Thermal conductivity of the liquid, W m^{-1} K^{-1}
Nu	Nusselt number
Nu_i	Local Nusselt number based on inlet radius, $h_i r_o/k_l$
$\overline{Nu}$	Average Nusselt number
Pe	Peclet number, Re Pr
Pr	Prandtl number
q_o	Heater input power per unit area, W
$\dot{Q}$	Total heat input power, W
r_o	Liquid inlet collar radius, m
$\tilde{r}$	r/r_o
R	Bubble radius, m
$\tilde{R}$	Dimensionless bubble radius, R/h_o
Re	Inlet Reynolds number, $u_o r_o/\nu$
s	Height of temperature Zone I, m
$\tilde{s}$	Dimensionless height of temperature Zone I, s/h_o
T	Temperature, K
T_b	$\frac{k}{q_0 h_0}(T_e\|_0 - T_{sat})$
T_e	Temperature of fluid film just prior to encountering a bubble, K
T_o	Disk inlet temperature, K
T_{sat}	Saturation temperature of water, K
T_{wi}	Local disk surface temperature, K
u_b	Bubble velocity, m s^{-1}
u_o	Radial velocity component at the exit of the collar, m s^{-1}
u_r	Radial velocity of water film on the disk, m s^{-1}
$\tilde{u}_r$	Dimensionless radial velocity u_r/u_o
u_{slip}	Bubble slip velocity, $u_b - u_r(\delta_b)$
u_x	Microfilm velocity underneath a bubble
$\tilde{u}_x$	Dimensionless velocity in the x direction, u_x/u_b
U	Bubble analysis variable
$\tilde{x}$	Dimensionless distance along the bubble, x/R
$\tilde{z}$	Dimensionless height, z/h_o

Greek symbols

ν	Kinematic viscosity of the liquid, m^2 s^{-1}
δ	Liquid film height, m
δ_b	Bubble height, or microlayer thickness, m
$\tilde{\delta}_b$	Dimensionless bubble height, δ_b/h_o
θ_b	Dimensionless temperature in the microlayer, $(k/q_0 h_0)(T-T_{sat})$

disk rotation speeds. They found that increasing the wall superheat increased the intensity of the boiling. As the boiling became more intense, the influence of water flow rate on the heat transfer coefficient decreased. Increasing the rotation rate of the disk also decreased the influence of flow rate on heat transfer. Yanniotis and Kolokotsa reported area-averaged heat transfer coefficients up to 16 kW/m^2K.

Another way to characterize flow boiling is to study how sliding bubbles behave and how they enhance heat transfer. Numerous researchers have investigated the mechanisms involved in nucleate boiling heat transfer in general and the influence of sliding bubbles in particular. Sliding bubbles have been shown to enhance heat transfer through mixing of the bulk fluid and creation of a microlayer underneath the bubbles. Kenning, Bustnes and Yan [4] used liquid crystal thermography and a multi-part model to determine the heat transfer rate to a sliding bubble surrounded by the constituent fluid. Their experimental setup used a heated, downward facing plate at a 15 degree angle in contact with saturated water. A thermochromic liquid crystal layer was applied on the top side of the plate to allow for visualization of temperature variations caused by sliding bubbles. An analytical model was also constructed taking into account the microlayer of water between the bubble and the plate, the contact area at the leading edge of the bubble, and the inviscid flow over the remainder of the bubble. They chose to use a reference frame fixed to the bubble and accounted for the thermal capacity of the inclined heater plate. Experimental data were utilized in conjunction with the model to determine the microlayer thickness, suggesting a layer thickness of 40–80 μm. The model predicted that the existence of the microlayer contributed very little to the enhanced heat transfer observed from the bubble. Most of the improvement in the heat transfer rate was predicted to arise from other fluid dynamics associated with sliding bubbles.

More recently, Bayazit, Hollingsworth and Witte [5] used a setup similar to that of reference [4] to measure the heat transfer enhancement from a sliding bubble on a downward facing heater surface. They used Fluorinert FC-87 for their liquid, a heater surface inclination of 12 degrees from the horizontal and thermochromic liquid crystal thermography. They too modeled the heat transfer into the sliding bubble, taking into account the thermal capacity of the heater surface. However, their model only focused on the microlayer of fluid underneath the bubble and ignored the additional forms of heat transfer enhancement caused by the bubble. The model assumed linear velocity and temperature profiles in the microlayer. The model results were matched to the experiments by adjusting the microlayer thickness used in the model. Thicknesses of 35–58 μm resulted in good agreement between the measured and the modeled wall temperatures.

Hollingsworth, Li and Witte [6,7] continued the investigation into sliding bubbles by using laser imagery to directly measure the microlayer thickness below sliding bubbles of FC-87. In their experiments they found that increasing the speed of the bubbles relative to the plate decreased the microlayer thickness. Results for the microlayer thickness ranged from 22 to 55 μm for plate inclinations between 2 and 15 degrees. The microlayer thickness was also found to be relatively constant from the leading to the trailing edge of the bubble. A new model was formulated based on one constructed by Addlesee and Kew [8], but modified to take into account that not all of the water at the leading edge of the bubble transfers to the microlayer and that some of the microlayer liquid evaporates. Experimental data were utilized to calibrate the model by adjusting the quantity of fluid that transferred to the microlayer. The model successfully predicted the relatively constant thickness of the microlayer.

Heat transfer in falling films has generated a significant amount of interest, including research into sliding bubbles produced during nucleate boiling. Falling films have thin fluid layers with a free surface that can sustain hemispherical bubbles that protrude out of the surface. The bubbles slide with the liquid film and enhance the heat transfer due to the same mechanisms cited in [4–8]. Fujita and Ueda [9] performed a series of boiling heat transfer experiments using water flowing down a vertical annulus at atmospheric pressure. Their goal was to gather data on the heat transfer coefficient and droplet entrainment rate for the falling film up to the point of

film breakdown. They found that at low heat fluxes they produced few bubbles and their data closely matched predictions from Chun and Seban [10] for evaporating water films flowing down the outside of a tube. When high enough heat fluxes were applied to the annulus, fully developed nucleate boiling occurred, at which point their data closely matched predictions from McAdams [11] for forced convection nucleate boiling. In addition, they found that once fully developed nucleate boiling occurred the heat transfer coefficient was no longer affected by the water flow rate.

Cerza [12] also studied nucleate boiling in thin falling water films. His experimental setup was centered on a heated, vertical brass tube with water saturation temperatures of 90 °C and 100 °C. Heat fluxes ranged from 6 to 78 kW/m^2 and film Reynolds numbers ranged from 640 to 5000. Visualization of the flow allowed the experimental data to shed light on the phenomena of bubble initiation and bubble growth. Cerza created a model to predict the heat transfer into the base of the bubble and the bubble growth rate. This model used a reference frame attached to the bubble, assumed a hemispherical bubble shape, infinite thermal capacity of the tube, a parabolic velocity profile in the microlayer and an initially linear temperature profile in the microlayer. The temperature profile in the microlayer is dictated by the solution of the differential equations, which, unlike Bayazit, Hollingsworth and Witte's model, captures the enhanced heat transfer that takes place at the leading edge of the bubble. Like most other researchers, Cerza used his model to determine what the microlayer thickness might have been in the experiments by adjusting the model's microlayer thickness until the bubble growth rate matched experimental data. He found that a micro layer thickness of 60 μm resulted in good agreement between his model and his experiments.

2. Experimental

2.1. Rotating disk setup

The experimental setup utilized in the study reported by Ozar et al. [13] was modified for the present study. A schematic of the experimental setup is shown in Fig. 1. The 40.6 cm diameter 6061 aluminum disk was mounted onto a precision stainless steel spindle. Deionized water was pumped through a rotating coupling into the hollow spindle and directed water onto the disk from the flow collar. The collar extended a radial distance of 5.1 cm from the center. It also served to make the flow circumferentially uniform, and ensured a fully developed Poiseuille velocity profile. The vertical distance between the disk and the collar could be adjusted, but was set to 0.254 mm for these experiments. After the fluid flowed over the disk, it was collected by an annular tank. The liquid flow rate was controlled with large and small metering valves, while the volumetric flow rate was measured by an in-line turbine flow meter (±0.3 lpm). A flat etched foil heater (Minco Inc., Minneapolis, MN) with a maximum heat input rate of 6.7 kW was installed in the disk, and insulated on the bottom side. Attempts to increase the heat input beyond 6.7 kW resulted in frequent heater burnouts and therefore could not be employed in the reported experiments. The heater had an outside diameter of 35.6 cm and inside diameter of 10.2 cm, which was the same as the outside diameter of the collar. The heater was powered by a 440 V variable AC transformer. A power slipring (UEA Inc., Waverly, IA) was used to transmit electrical power to the rotating disk-heater assembly.

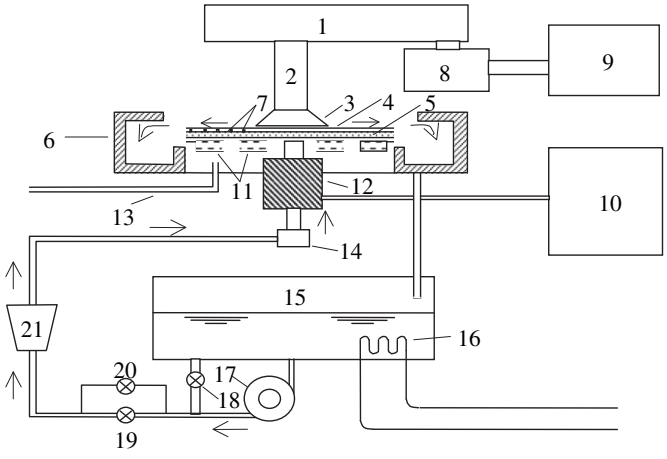

Fig. 1. Rotating disk setup for heat transfer experiments of a controlled liquid impinging jet. (1) Pulley assembly, (2) High precision spindle, (3) Flow collar, (4) Disk, (5) Etched foil heater, (6) Annular tank, (7) Thermocouples, (8) Motor, (9) Variable speed motor control, (10) 0–500 V heater control, (11) Thermocouple amplifiers, (12) Precision slip ring, (13) Cooling air, (14) Rotating coupling, (15) External process tank, (16) Heat exchanger, (17) Bypass valve, (18) Bypass valve, (19) Large metering valve, (20) Small metering valve, (21) Flow meter.

Temperature measurements were taken of the aluminum disk at seven radial locations. The temperature measurement system consisted of seven T-type thermocouples (with typical measurement accuracy of ±0.5 °C), installed in 1.6 mm diameter holes drilled on the underside of the disk, terminating at a depth of 3.81 mm away from the upper disk surface. They were located at radii of 7, 7.9, 8.9, 10.8, 12.7, 14.6 and 16.5 cm away from the disk center and were cemented in their location using high thermal conductivity cement (Omega, OB-400). Voltage signals from the thermocouples were converted to electrical current using thermocouple transmitter modules installed under the rotating disk and passed through a precision slip ring. This arrangement eliminated the electrical noise that would have occurred if low voltage signals were transmitted through the slip ring. The transmitter assembly consisted of seven Watlow WG5900 transmitters (±0.02 °C span, ±0.3 °C ambient temperature effects, and ±0.02 °C cold junction compensation) mounted on to a low thermal conductivity phenolic plate underneath the disk. These transmitters were extensively checked for the linearity of the input and output characteristics during temperature calibrations. An 18 conductor precision slip ring, manufactured by IEC Corp. of Austin, TX, was mounted to the spindle in the annular space and transmitted the electrical signals from the thermocouple transmitters. The slip ring was tested for conductor crosstalk and impedance variation, both of which were found to be negligible. Shunt resistors (250 Ω) were used to convert the 4–20 mA current output of the thermocouple transmitters to 1–5 V output signal across appropriate shunt resistors. The voltage signals were measured with a Fluke model 2625A data logger. An additional T-type thermocouple was used to measure the inlet temperature just before the fluid flows into the spindle. A heater was placed in the water tank to make up for thermal losses in the supply lines.

2.2. Experimental test conditions

Heat transfer measurements for the boiling experiments were taken with a heater power of 6700 W (73.46 kW/m^2). Rotational speed of the disk was varied from 0 to 100 rpm with an uncertainty of ±1 rpm. Water flow rates of 3.0 lpm, 7.0 lpm and 12.0 lpm (±2.5%) were considered. Disk surface temperatures were determined from the measurements using a one-dimensional heat conduction model to extrapolate the measured temperatures to the disk surface. The extrapolation included the effect of the anodized surface. The maximum correction for the surface temperature was less than 0.25 °C in all of the experiments. Water properties were evaluated at the inlet temperature. Table 1 contains a summary of the experimental conditions employed in this study.

Table 1
Test conditions and cases.

	Heating
Inlet temperature (°C)	94.6–99.1
Collar height (mm)	0.254
Water flow rate (l/min)	2, 3, 4, 7, 12
Rotation rates (rpm)	0, 25, 50, 100
Heater power (W)	6700
Reynolds number	70 000–420 000
Prandtl number	1.76
Peclet number	1×10^5–7×10^5

The ambient air over the disk setup was kept still so that the thermal and mass boundary layers above the water surface were dominated by the water film temperature rather than the conditions of the ambient medium. An analysis of the heat transfer into the still air above the disk revealed that heat loss due to convection was at most 1% of the overall heater power. Variations in the room temperature would have caused only a 0.2% variation in the overall temperature of the water film, which was deemed small enough to ignore. Similarly, variations of the humidity in the room were also ignored. Changing the dew point in the room from −10 to 30 °C creates a change in water vapor concentration gradient of only 4% when the water film is at 100 °C, so that the humidity levels in the room surrounding the experiment did not affect the results.

Flow visualization and characterization of the nucleate boiling on the disk was accomplished by the use of a Motion Scope Model PCI 80005 CCD video camera (Redlake Imaging Corporation). Fig. 2 shows the setup of the video camera relative to the rotating disk. The camera was set about 68 cm from the disk at an angle of 45-degrees from the vertical (to keep steam off the lens). A 25 mm lens was used and the disk was illuminated with a high intensity arc lamp. The camera was setup to operate with a shutter speed of 1/500 s at a framing rate of 500 frames per second. The area viewed by the camera corresponded to a 7.6 cm by 7.6 cm region with a pixel format of 320 × 280 pixels. Video data were studied frame by frame, and software tools were used to measure the size of the bubbles within each frame. The size, population and growth rate of the bubbles were measured and fed into the analytical models.

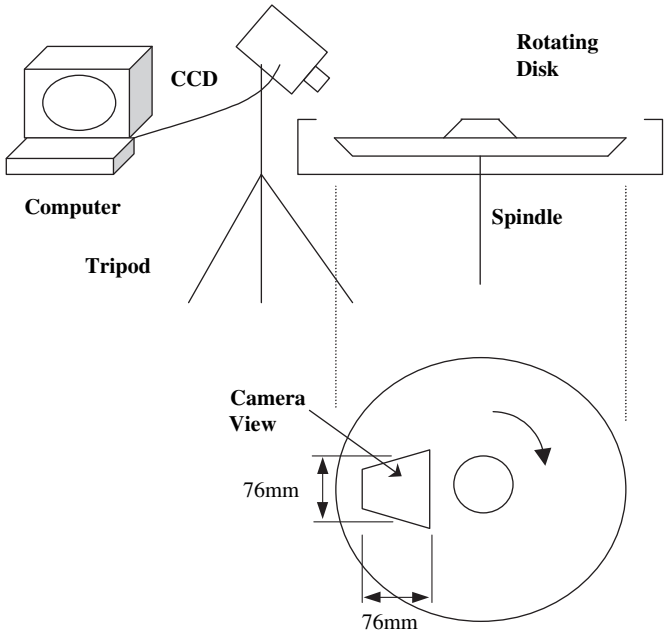

Fig. 2. CCD camera setup.

2.3. Experimental procedure

Experiments were initiated by turning on the water pump and setting the metering valves to the desired flow rate. The disk heater was turned on next and the heating rate slowly increased to 6700 W. The tank immersion heater was turned on and set to regulate the water temperature at 100 °C. Heat transfer data were then obtained once the water reached 90 °C as determined by the disk water inlet temperature. The inlet water was held to 97.0 °C ± 2.5 °C over the course of the evaporation experiments. Temperature and power data were taken at fifteen-minute intervals for each test condition until the maximum change in any of the local Nusselt number calculations was less than 2% and the average Nusselt number change was less than 1% from the previous reading. Each experiment was carried out for a minimum of 45 min. The rotation rate of the disk was increased from stationary to the highest rotation rate at each flow rate. Flow rates of 2 lpm, 3 lpm, 4 lpm, 7 lpm and 12 lpm were employed, beginning with the 12 lpm cases. Repeats of the tests showed that the order of the flow rate and disk rotation conditions did not influence the heat transfer data.

2.4. Method of data analysis

The temperature and power data were used to calculate the local and average Nusselt numbers for the disk. The local heat transfer coefficient was calculated as

$$h_i = (\dot{Q}/A_h)/(T_{wi} - T_o), \tag{1}$$

where $\dot{Q}$ is the total heat input to the disk from the heater, A_h is the heated disk area, T_{wi} is the disk surface temperature, and T_o is the water temperature at the inlet collar. The index "i" identifies the discrete locations of temperature measurements. This analysis assumes uniform heat flux into the disk. Non-uniformities in the heat flux would affect the calculation of the Nusselt number, thus the uniformity of the heat transmitted in the heater-disk assembly was checked in several ways. First, an IR camera was used to view the heated, still disk without water present in an attempt to find hot or cold spots. None were found. Second, thermocouples were placed at a dozen different locations on the disk surface and the disk edge was built up to hold still water. When the heater was turned on, even temperatures (within the instrument uncertainty) were recorded on the disk, suggesting that heat was supplied uniformly onto the disk.

The local Nusselt number was calculated from the local heat transfer coefficient and the inlet radius of the disk such that

$$Nu_i = (h_i r_o/k_l). \tag{2}$$

where k_l is the liquid conductivity. The disk inlet radius was chosen as the practical length scale in the Nusselt number definition as it has been also used in other studies [13–15]. The average Nusselt number was calculated using an area-weighted average of the local Nusselt numbers as,

$$\overline{Nu} = \frac{\sum_{i=1}^{7} Nu_i \times A_i}{A_h}. \tag{3}$$

The total area of the disk was divided into seven rings, A_i, with each containing one of the thermocouples. Rice et al. [14] and Basu and Cetegen [15] also used this method of calculating an area-weighted average of the heat transfer coefficient.

The uncertainty in the Nusselt number was estimated to be about ±14% for the experiments. Most of this uncertainty arose from using the difference between two thermocouple readings

during the calculation of the Nusselt number (Eq. (1)). Each temperature reading on the disk had an uncertainty of ±1.8 °C, which took into account the uncertainties from the thermocouple itself all the way through the Fluke data logger output.

Flow visualization videos were taken at 500 fps for all of the test conditions. Scale calibration was done by placing a ruler on the disk in the radial direction and recording its image. The height of the video frame was determined to the closest millimeter distance. The width of the frame was taken at the midpoint of the imaged trapezoidal region. Analysis of the video frames was performed with the aid of the camera's software's measuring tool. A sample of 2–4 segments were taken from the video clips and analyzed for bubble frequency and bubble growth rate. Bubble size and population density was gathered by examining every 50th frame, which equated to a frame every 0.1 s.

The experimental study was complemented by applying the integral analysis of Basu and Cetegen [15] to a sliding bubble model similar to the one developed by Cerza [12]. This analysis predicted the growth rate of a sliding bubble and the associated increase in the local Nusselt number. The analysis is presented in the following section.

3. Sliding bubble analysis

A computational analysis was performed of the thin liquid film below a single sliding bubble. The goal of this analysis was to use an integral method to determine the approximate bubble growth rate and the increase in Nusselt number beneath the bubble. The integral analysis was based on the method described in Basu and Cetegen [15] while the model of the sliding bubble was based on the work of Cerza [12].

The bubble analysis was conducted using a parabolic velocity profile and a two-zone linear temperature profile as shown in Fig. 3. The conservation equations were integrated from the disk surface to the lower bubble boundary. The dual linear temperature profile captures the phenomenon of a steep temperature gradient at the leading edge of the bubble without creating a large discontinuity in temperature or disk heat flux. Effects of evaporation in the bubble base were captured by the depth of Zone II shown in Fig. 3. Once Zone II spans the entire distance from the bubble base to the disk surface, Zone I disappears. At that point, it is assumed that the disk has an infinite heat capacity so that the temperature remains constant, but the heat flux increases to match the slope of the temperature profile in Zone II. An extension of this integral analysis could utilize a constant heat flux boundary condition and determine the temperature change at the disk surface. Such an extension would increase the accuracy of the analysis by taking into account the thermal capacity of the disk as well as its thermal diffusivity.

The assumptions utilized in the analysis are listed below. Those that are common with Cerza are marked with a (C).

1) Analysis assumes quasi-steady bubble growth rate such that changes in radius, temperature, disk film thickness and overall fluid velocity are not considered.
2) Two-dimensional Cartesian coordinates were used as shown in Fig. 3, with no energy or mass flux in the direction of rotation (y direction).
3) Fluid properties were assumed to be constant.
4) The bubble's boundary with the water film was at the saturation pressure. (C)
5) A quadratic velocity profile existed under the bubble with a zero-shear condition at the base of the bubble. (C)
6) The temperature profile in the water film under the bubble could be approximated using two intersecting linear profiles.
7) Radial growth of the bubble boundary was small compared with the bubble slip velocity and could be ignored. (C)
8) Evaporation of the bubble base was small enough that the base could be assumed to be constant thickness. (C)
9) The bubble traversed the disk at a constant film thickness. (C)
10) Heat transfer between the liquid film and bubble was only significant at the bubble's base. (C)
11) The growing bubble remained hemispherical. (C)
12) The disk surface temperature remained constant.

3.1. Governing equations

Simplified governing equations under the stated assumptions are given below. They reflect several simplifications. First, the problem is being treated as quasi-steady state, so that time derivatives vanish. The assumption of constant bubble base thickness also simplifies the governing equations since velocities normal to the disk surface (z-direction) and its derivative vanish. Finally, the pressure change in the direction of bubble motion ('x'-direction) is considered to be negligible. The continuity equation then becomes

$$\frac{\partial u_x}{\partial x} = 0. \tag{4}$$

Incorporating the continuity equation in the x-momentum equation shows that the velocity profile is invariant with x. Applying the boundary and initial conditions, one obtains the velocity profile normal to the disk surface, and the x-momentum equation drops out. These simplifications lead to the energy equation of the form,

$$u_x \frac{\partial T}{\partial x} = \alpha \left[\frac{\partial^2 T}{\partial x^2} + \frac{\partial^2 T}{\partial z^2} \right]. \tag{5}$$

The equations are non-dimensionalized as defined in the nomenclature, resulting in,

$$\text{Continuity} : \frac{\partial \tilde{u}_x}{\partial \tilde{x}} = 0 \tag{6}$$

$$\text{Energy} : \tilde{u}_x \frac{\partial \theta_b}{\partial \tilde{x}} = \frac{1}{Pe \times \tilde{R}} \left[\frac{\partial^2 \theta_b}{\partial \tilde{x}^2} + \tilde{R}^2 \frac{\partial^2 \theta_b}{\partial \tilde{z}^2} \right] \tag{7}$$

A scale analysis shows that the streamwise conduction term can be ignored, simplifying the energy equation as:

$$\tilde{u}_x \frac{\partial \theta_b}{\partial \tilde{x}} = \frac{\tilde{R}}{Pe} \frac{\partial^2 \theta_b}{\partial \tilde{z}^2} \tag{8}$$

3.2. Liquid film hydrodynamics

Cerza [12] suggested that the radial velocity under the bubble takes the form of a second order polynomial,

$$\tilde{u}_x = a_o + a_1 \tilde{z} + a_2 \tilde{z}^2. \tag{9}$$

In addition, it is more convenient to transform from a disk coordinate system to a coordinate system attached to the bubble. From the bubble coordinate system, the disk is moving forward with respect to the film of water underneath it. The velocity profile is schematically shown in Fig. 3. The bubble moves with a velocity, u_b with respect to the disk, with bubble velocity measured from experimental data. The bubble base moves at a certain speed with respect to the fluid layer it encounters as $u_{\text{slip}} = u_b - u_r(\delta_b)$.

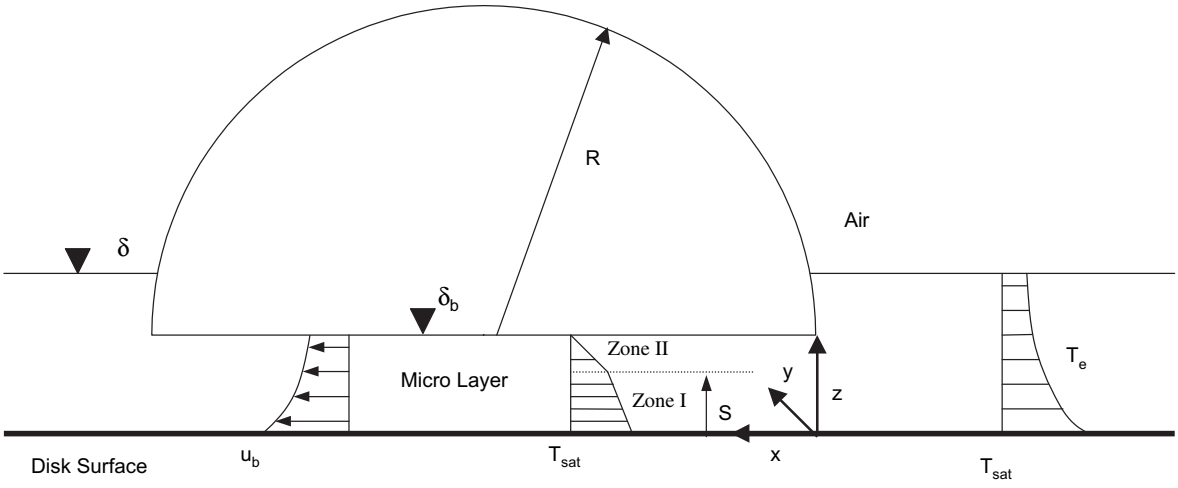

Fig. 3. Sliding bubble model for the integral analysis.

The boundary and initial conditions for the hydrodynamics are

1) Disk moves with velocity u_b:

$$\tilde{u}_x(\tilde{z}=0) = 1 \tag{10}$$

2) No shear at bubble boundary:

$$\frac{\partial \tilde{u}_x}{\partial \tilde{z}}(\tilde{z}=\tilde{\delta}_b) = 0 \tag{11}$$

3) Velocity at the bubble base is equal to the velocity of fluid that the bubble encounters minus the bubble velocity:

$$\tilde{u}_x|_{\tilde{\delta}_b} = 1 - \frac{u_o}{u_b}\tilde{u}_r|_{\tilde{\delta}_b} \tag{12}$$

where $\tilde{u}_r|_{\tilde{\delta}_b}$ is found from the disk analysis described by Quinn [16]. Applying the boundary conditions yields a velocity profile under the bubble, which is completely defined and equal to

$$\tilde{u}_x = 1 - 2\frac{U}{\tilde{\delta}_b}\tilde{z} + \frac{U}{\tilde{\delta}_b^2}\tilde{z}^2 \tag{13}$$

with $U = (u_o/u_b)\tilde{u}_r|_{\tilde{\delta}_b}$.

3.3. Energy equation

The energy equation is solved by first integrating it with respect to '*Z*', then substituting in the appropriate velocity and temperature profiles. For this analysis, the temperature profile underneath the bubble was divided into two zones, as shown in Fig. 3. Each zone has a linear temperature profile. The temperature of Zone I is fixed and invariant with respect to '*x*'. Its value at the disk surface is found from the analysis conducted by Quinn [16] and reflects the amount of superheat needed to reach boiling. The slope of the temperature profile in Zone I is set by the power applied to the disk heater. The temperature of Zone II is fixed to the saturation temperature at the bubble interface and the temperature of Zone I at the point where the two zones intersect. At the leading edge of the bubble, Zones I and II intersect just below the bubble base, which creates a very steep temperature gradient in Zone II. Applying the boundary conditions to the two zones yields the following two temperature profiles.

$$\theta_{b1} = T_b - \tilde{z} \tag{14}$$

$$\theta_{b2} = \frac{(\tilde{z}-\tilde{\delta}_b)}{(\tilde{s}-\tilde{\delta}_b)}(T_b - \tilde{s}) \tag{15}$$

with

$$T_b = \frac{k_l}{q_0 h_0}(T_e|_0 - T_{\text{sat}}) \tag{16}$$

These profiles are substituted into an integral form of the energy equation and arranged such that the height of Zone I, '*s*', is the dependent variable. The final form of the energy equation becomes,

$$\frac{d\tilde{s}}{d\tilde{x}} = \frac{\tilde{R}}{Pe}\left(\frac{(T_b-\tilde{s})}{(\tilde{s}-\tilde{\delta}_b)}+1\right)\left(B - \frac{A}{\tilde{s}-\tilde{\delta}_b} - A\frac{T_b-\tilde{s}}{(\tilde{s}-\tilde{\delta}_b)^2} + C\frac{T_b-\tilde{s}}{(\tilde{s}-\tilde{\delta}_b)}\right)^{-1}$$
$$\text{with } A = \tilde{\delta}_b^2\left(\frac{U}{4}-\frac{1}{2}\right) + \tilde{\delta}_b\tilde{s} - \tilde{s}^2(U+\tfrac{1}{2}) + \tilde{s}^3\frac{U}{\tilde{\delta}_b} - \tilde{s}^4\frac{U}{4\tilde{\delta}_b^2},$$
$$B = T_b - \tilde{s}\left(\frac{2T_bU}{\tilde{\delta}_b}+1\right) + \tilde{s}^2\left(\frac{T_bU}{\tilde{\delta}_b^2}+\frac{2U}{\tilde{\delta}_b}\right) - \tilde{s}^3\frac{U}{\tilde{\delta}_b^2} \text{ and}$$
$$C = \tilde{\delta}_b - 2\tilde{s}(U+\tfrac{1}{2}) + 3\tilde{s}^2\frac{U}{\tilde{\delta}_b} - \tilde{s}^3\frac{U}{\tilde{\delta}_b^2}. \tag{17}$$

The energy equation is solved using a fourth order Runge–Kutta routine that marches from the leading edge of the bubble to its trailing edge. The bubble is divided into several chords as shown in Fig. 4. Inlet conditions of the chords are identical to each other. The heat transferred into the bubble at each step of each chord is summed up to yield the total heat transferred into the bubble. This quantity is translated into the rate of growth of the bubble radius.

3.4. Grid independence

Two grid studies were conducted to demonstrate grid independence of the analysis. A round bubble was discretized in both '*x*' and '*y*'. The *x* direction is the direction of bubble motion. The bubble analysis marches from the leading edge of the bubble ($x = 0$) to its trailing edge ($x = 2$) with a step size of *dx*, where *x* has been non-dimentionalized with respect to the bubble radius, *R*. The bubble analysis also segments the bubble into longitudinal strips, or

chords. Each chord has a width of $d\tilde{y}$. The longest chord is the one in the center of the bubble, with a length of $2 \times R$.

Fig. 5 shows the amount of heat absorbed by the center strip of the bubble, given different values of dx. All grid sizes that were utilized resulted in similar heat flux values. For a good mix of accuracy and computational efficiency, $d\tilde{x} = 0.005R$ was chosen for subsequent analyses. The computed heat flux and computational efficiency were found to be less sensitive to the grid resolution in the y direction. Analyses were carried out with $d\tilde{y} = 0.05R$ and $0.10R$ and the thermal energy absorbed by the bubble in each case was within 0.3% of each other. A grid size of $d\tilde{y} = 0.05R$ was chosen for subsequent analyses.

4. Results and discussion

Nusselt numbers for the evaporation and boiling experiments are shown in Fig. 6. The boiling experiments produced average Nusselt Numbers that were higher than those attained in the evaporation experiments described in Quinn [16] for the 3 lpm and 7 lpm cases, and matched the data for the 12 lpm case. These results suggest that boiling effects the Nusselt numbers most at the lower flow rates and lower rotation rates. All of the 3 lpm boiling data showed large increases in the average Nusselt Number compared with the 3 lpm evaporation data. The 7 lpm flow rate, stationary disk case also showed a large increase in average Nusselt Number, while the 7 lpm boiling data with rotation showed a moderate increase in average Nusselt numbers. The 12 lpm boiling data were almost the same as the 12 lpm heat transfer data taken for the evaporation experiments regardless of the rotation rate. This suggests that no substantial boiling was taking place in the 12 lpm "boiling" experiments, which was also visually confirmed.

The data show that boiling would only occur if the disk surface superheat was 25 °C or higher. This level of superheat falls into the high end of the range for boiling to occur, which typically require from 5 to 30 °C superheat. The requirement for a large superheat meant that experiments with supercritical (thin film) flow had the least vigorous boiling because the disk temperature was lower as compared to other experiments. Conversely, experiments with subcritical (thick film) flows had rapid boiling which greatly affected the heat transfer rates.

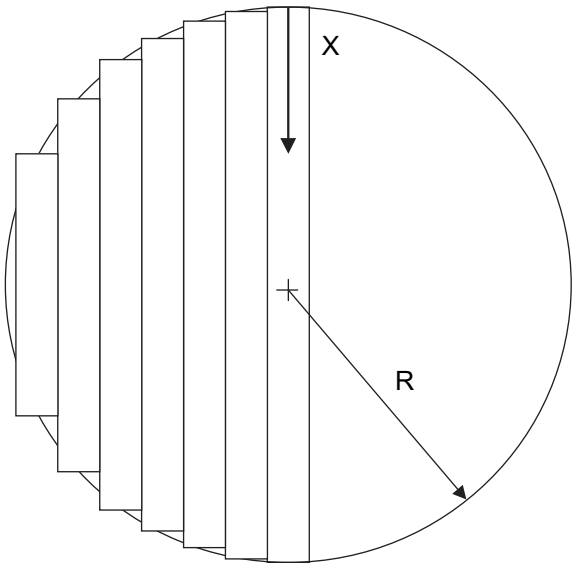

Fig. 4. Discretization of a bubble using chords of varying length.

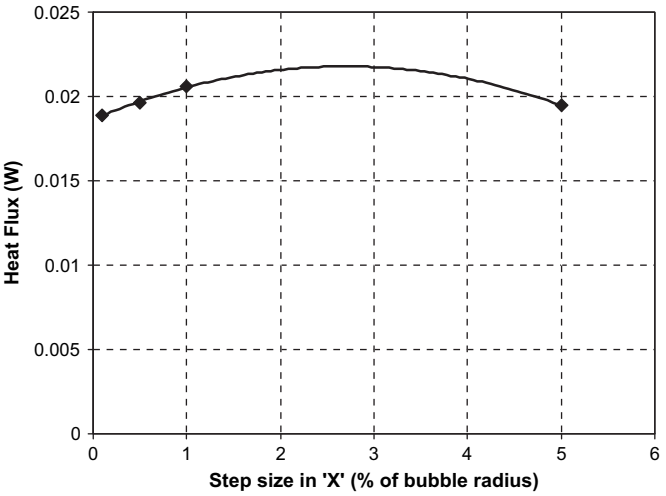

Fig. 5. Sensitivity of heat flux into the center chord as a function of grid size.

Fig. 7 shows the distribution of bubble sizes for each experiment conducted with disk rotation. These data were gathered by measuring the number and size of each bubble seen in ten frames of video taken during the experiments. The figure shows that the median bubble diameter for the experiments was about 6 mm. Fig. 8 shows how the flow rate and rotation rate affect the size and quantity of bubbles present for the $\omega = 25$ rpm and $\omega = 50$ rpm

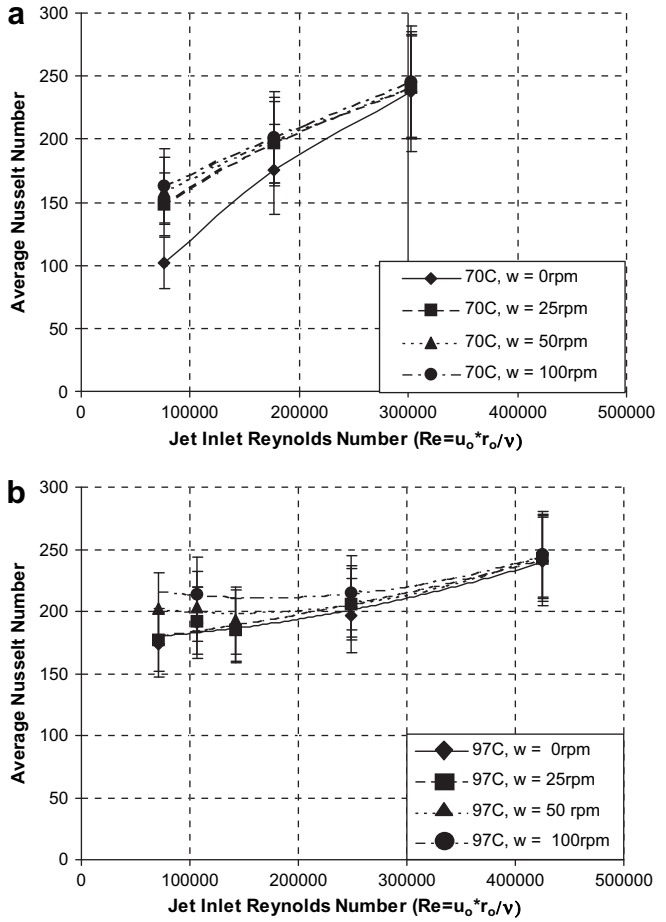

Fig. 6. Area-weighted average Nusselt Numbers for evaporation (a) and boiling (b).

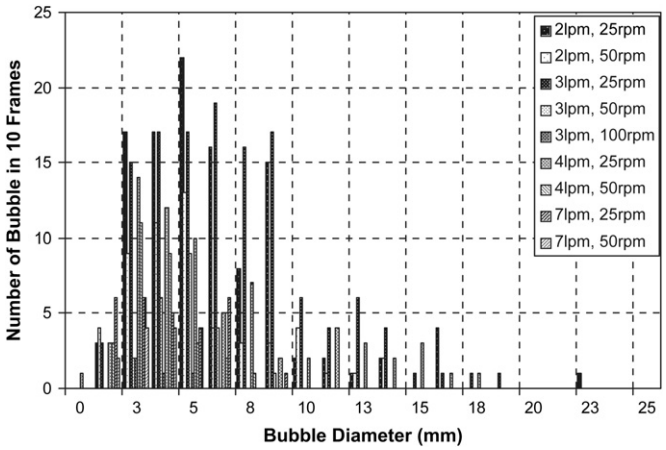

Fig. 7. Histogram of bubble size and frequency for boiling experiments with rotation.

experiments. Increasing the flow rate and the rotation rate tended to decrease the average bubble diameter and decrease the number of bubbles present on the disk at any particular moment. Bubble nucleation frequency was also measured and found to range from 63 to 147 Hz, with no clear dependence on flow or rotation rate. The nature of the bubbles formed in subcritical, supercritical and transitional flow regimes differed from each other in quantity, size, movement, and spacing such that each region's boiling characteristics warrant a more detailed analysis.

Subcritical flow regions had lower heat transfer coefficients and higher disk temperatures than areas with supercritical flow. As a result, they produced the most rapid boiling. Fig. 9a shows a picture of subcritical flow boiling, where the bubbles are tightly packed together and quite large. This type of densely packed bubbles was difficult to analyze with the high-speed camera

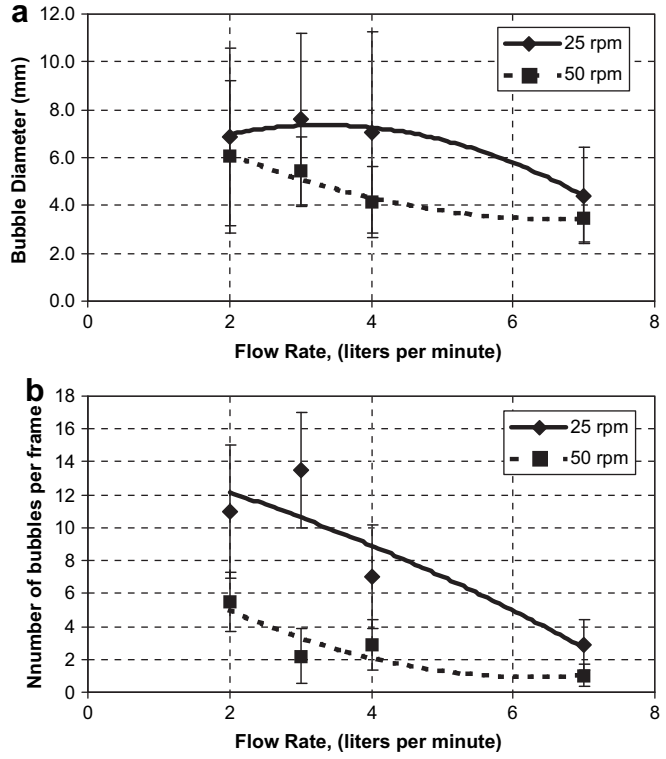

Fig. 8. (a) Bubble size and (b) bubble quantity for $\omega = 25$ rpm and for $\omega = 50$ rpm.

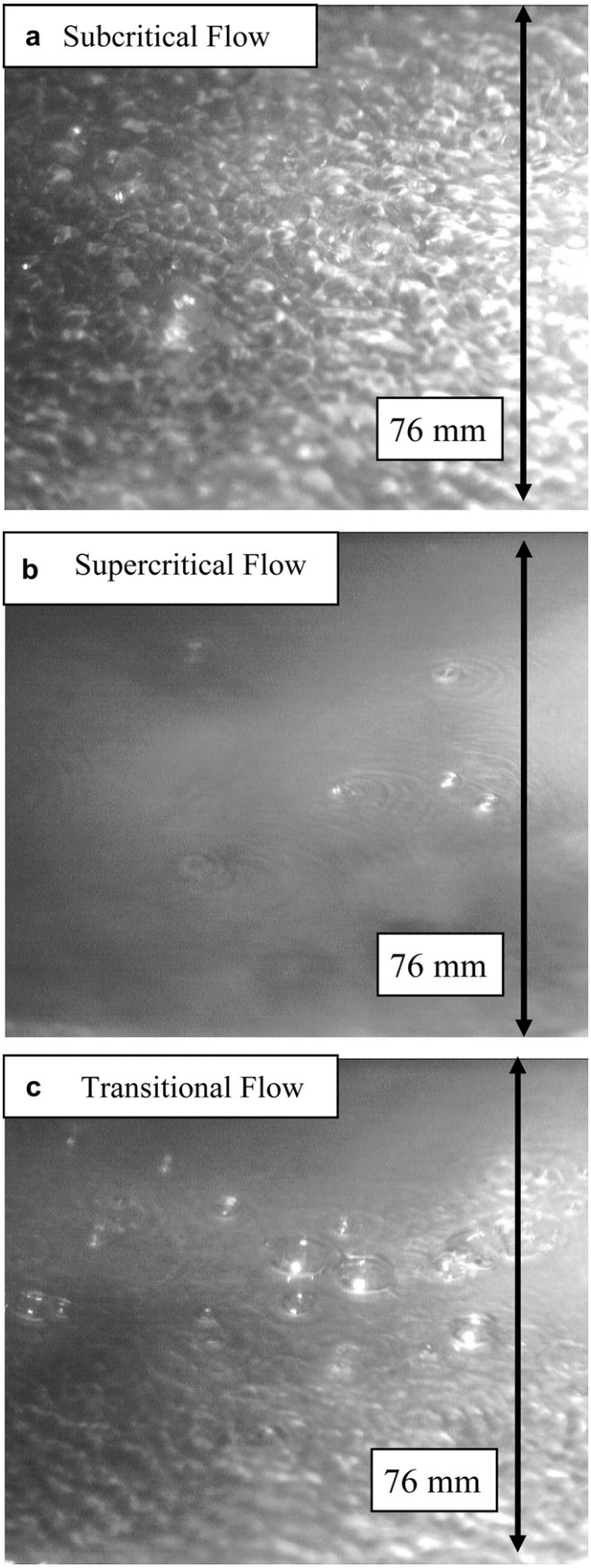

Fig. 9. Pictures of three primary types of boiling in (a) subcritical flow, (b) supercritical flow, and (c) transitional flow.

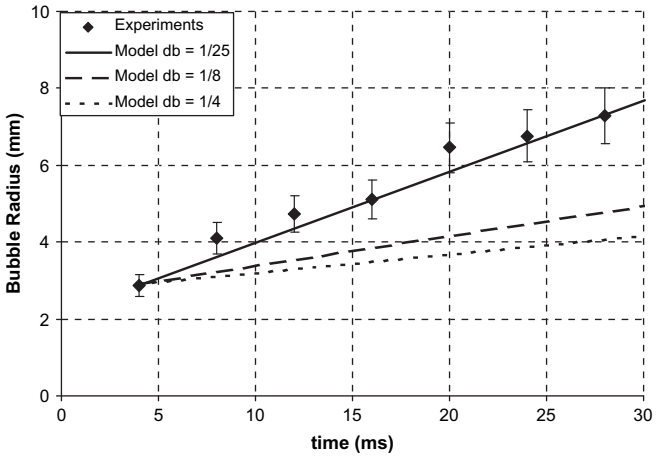

Fig. 10. Individual sliding bubble growth rate for 3 lpm, $\omega = 25$ rpm experiment.

because distinct bubbles could rarely be identified among the churning waves. However, some general observations of the nature of the subcritical boiling were made. First, bubbles found in the subcritical region were typically large, fixed in place, and burst rapidly. Second, several instances of bubbles merging with each other were observed. Smaller bubbles sometimes floated on top of the water film in the subcritical flow region. These bubbles would occasionally collide with other bubbles and either burst or, less frequently, merge into one large bubble that would burst shortly afterwards.

Boiling in supercritical flow differed greatly from boiling in subcritical flows. Fig. 9b is a single frame from the high-speed video and shows how much smaller and more separated the bubbles were in the supercritical flow areas. All of the bubbles in supercritical flow were small and never became detached from to the disk surface. They typically burst before growing larger than 5 mm in diameter. These bubbles disturbed the flow around them, sending ripples out in all directions.

A third type of bubble was observed when the disk was rotated slowly to partially wash out the hydraulic jump between supercritical and subcritical flow regions. In these cases, large, hemispherical bubbles would form at the hydraulic jump, detach from the disk, and slide radially outward. Fig. 9c shows an image that contains this type of sliding bubble. Sliding bubbles were produced when the disk rotated at 25 rpm and flow was controlled from

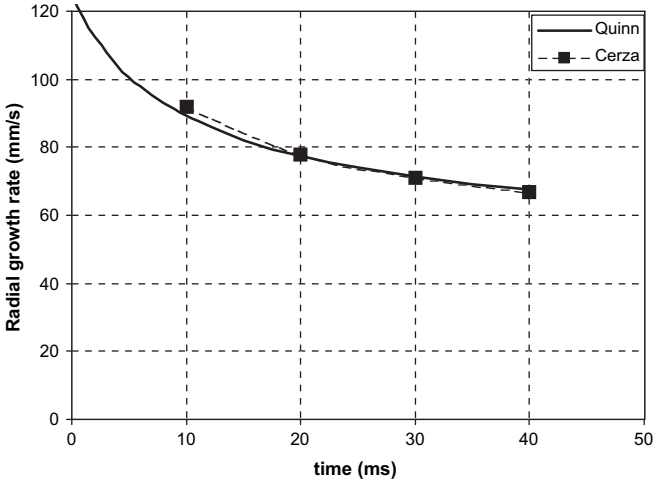

Fig. 11. Sliding Bubble analysis comparison between Quinn [16] and Cerza [12].

Table 2
Comparison of Nusselt numbers for 3 lpm, 25 rpm experiments.

	Nusselt number
Evaporation experiments (72 °C inlet)	148
Boiling data (100 °C inlet)	192
Sliding bubble analysis	3218
Increase in Nusselt number	23%
Percent coverage of disk with bubbles	1.4%

2 lpm up to 4 lpm. The growth rate of these sliding bubbles was measured, and bubble radii were found to increase linearly with time until the bubbles burst after about 28 ms. Fig. 10 shows the radius of a representative bubble at several time steps.

Results from the integral analysis of the microlayer underneath a sliding bubble were first compared with Cerza's results to determine how well it matched the full mathematical model of a sliding bubble. The results are plotted in Fig. 11 and show very good agreement between Cerza's model and the simpler integral analysis. The obtained experimental data were then utilized to determine the thickness of the microlayer underneath the sliding bubbles predicted from the integral model. Microlayer thickness, also known as bubble height, δ_b, was adjusted in the analysis until the predicted radial growth rate matched the growth rate found in the experiments. Fig. 10 shows predictions of the bubble analysis for several bubble depths. Cerza found that a microlayer thickness of ¼ of the film thickness accurately predicted the bubble growth rate in his falling film. However, a microlayer thickness of 1/25 of the film height gives a good match for the bubble growth rate in the present work. The microlayer height of 0.017 mm causes the temperature in the film underneath the bubble to quickly reach a linear profile as the bubble slides over superheated water and results in a linear bubble growth rate. This growth rate corresponds to a local Nusselt number under the bubble of $Nu = 3300$, which is significantly higher than the Nusselt number in the surrounding fluid, $Nu = 190$. The very thin microlayer also indicates that the increased Nusselt number associated with the bubble is dominated by the thickness of the micro layer, rather than by the leading edge encountering superheated water, as was the case in Cerza's analysis [12]. Performing an area-weighted average of the bubble Nusselt number and adding it to the evaporation Nusselt number from Quinn [16] suggests that sliding bubbles likely took up 1.4% of the area of the disk for the boiling experiments while increasing the overall Nusselt number by 28% (See Table 2).

5. Conclusions

Nucleate boiling of a controlled radially spreading jet on a rotating disk was investigated using experimental and analytical techniques. The experiments revealed that at a constant heat transfer rate, subcritical flow regions produced the most vigorous boiling. The thick film regions upstream of the hydraulic jump produced hemispherical sliding bubbles at slow rotation rates while supercritical flow regions downstream of the hydraulic jump produced small, rapidly bursting bubbles that disturbed the flow around them. As expected, the largest increases in the Nusselt number were obtained for the nucleate boiling conditions corresponding to the rapidly boiling subcritical flow regions. Conditions with flow rates and rotation rates that produced supercritical flow with thin films did not exhibit vigorous boiling and displayed the least amount of increase in heat transfer rates when compared with those for the lower temperature experiments.

The formulated integral analysis produced results that matched the full mathematical model reported by Cerza [12] quite well. When compared with experimental results from this study, the

analysis suggested that those sliding bubbles were embedded much deeper in the moving film than they were in Cerza's experiments. This shifts the primary heat transfer mechanism for bubble growth from the leading edge of the sliding bubble encountering superheated fluid to the extremely thin film below it, thus sustaining very high heat transfer rates. The analysis revealed that even a small number of sliding bubbles could greatly increase the overall heat transfer coefficient on the disk. Since these bubbles were typically produced at low flow rates and low rotation rates, producing them in an application such as a vapor absorption heat pump generator could result in power savings and size reduction.

Acknowledgments

The reported research was partially funded by the NASA Microgravity Fluids Physics Program, Glenn Research Center, Cleveland, Ohio, under contract number NCC3-789. The assistance provided by Saptarshi Basu with the experiments is kindly acknowledged.

References

[1] M. Anderson, D. Westheimer, Thermal Control System Development to Support the Crew Exploration Vehicle and Lunar Surface Access Module, NASA Technical Reports Server, ID No. 20080026002 (2006).
[2] I. Mudawwar, M.A. El-Masri, Boiling incipience in plane rotating water films. ASME J. Heat Transf. 110 (1988) 532–535.
[3] S. Yanniotis, D. Kolokotsa, Boiling on the surface of a rotating disc. J. Food Eng. 30 (1996) 313–325.
[4] D.B.R. Kenning, O.E. Bustnes, Y. Yan, Heat transfer to a sliding vapour bubble. Multiphase Sci. Technol. 14 (1) (2002) 75–94.
[5] B. Bayazit, D. Hollingsworth, L. Witte, Heat transfer enhancement caused by sliding bubbles. ASME J. Heat Transf. 125 (2003) 503–509.
[6] X. Li, D. Hollingsworth, L. Witte, The thickness of the liquid microlayer between a cap-shaped sliding bubble and a heated wall: experimental measurements. ASME J. Heat Transf. 128 (2006) 934–944.
[7] D. Hollinsworth, X. Li, L. Witte, The thickness of the liquid microlayer between a sliding bubble and a heated wall: comparison of models to experimental data. ASME J. Heat Transf. 130 (2008) 11501-1–111501-9.
[8] A.J. Addlesee, P.A. Kew, Development of the liquid film above a sliding bubble. Trans. IchemE Part C 80 (A3) (2002) 272–277.
[9] T. Fujita, T. Ueda, Heat transfer to falling liquid films and film breakdown – II, saturated liquid films with nucleate boiling. Int. J. Heat Mass Transf. 21 (1978) 109–118.
[10] K.R. Chun, R.A. Seban, Heat transfer to evaporating liquid films. ASME J. Heat Transf. 93 (4) (1971) 391–396.
[11] W.H. McAdams, C.S. Minden, R. Carl, D.M. Picornell, J.E. Dew, Heat transfer at high rates to water with surface boiling. Ind. Eng. Chem. 41 (1949) 1945–1955.
[12] M.R. Cerza, An Investigation into the Mechanism for Nucleate Boiling in Thin Falling Water Films, Ph.D. thesis, Rutgers University, New Brunswick, NJ, 1983.
[13] B. Ozar, Experiments on Hydrodynamic and Thermal Behavior of Thin Liquid Films Flowing Over a Rotating Disk, Masters thesis, University of Connecticut, Storrs, Connecticut, 2002.
[14] J. Rice, A. Faghri, B.M. Cetegen, Analysis of a free surface film from a controlled liquid impingement jet over a rotating disk including conjugate effects with and without evaporation. Int. J. Heat Mass Transf. 48 (2005) 5192–5204.
[15] S. Basu, B.M. Cetegen, Analysis of hydrodynamics and heat transfer in a thin liquid film flowing over a rotating disk by integral method. ASME J. Heat Transf. 128 (2006) 217–225.
[16] G. Quinn, Heat Transfer in a Liquid Film Flowing Over a Rotating Disk and a Diverging Channel with and Without Boiling and Surfactant Addition, Ph.D. thesis, University of Connecticut, Storrs, Connecticut, 2009.